Journal of Sound and Vibration 330 (2011) 1244–1264

Contents lists available at ScienceDirect

Journal of Sound and Vibration

journal homepage: www.elsevier.com/locate/jsvi

Transforming and separating rotating disk vibrations using a sensor array

Izhak Bucher*

Dynamics Laboratory, Mechanical Engineering, Haifa 32000, Israel

ARTICLE INFO

Article history:
Received 10 April 2010
Received in revised form
5 August 2010
Accepted 11 September 2010
Handling Editor: K. Shin
Available online 27 October 2010

ABSTRACT

This paper presents a method to separate the complex vibration pattern of a rotating disk into simpler entities. The decomposition transforms data measured by an array of sensors into time domain signals representing the contribution of individual modes of vibration. Having performed the decomposition with respect to wavelength, speed and direction of travel, the obtained measurements can be projected onto a rotating body experiencing variable rotational speed relative to the sensors. Unlike previous works, the vibrations here are decomposed into time domain signals that provide better insight into stress levels and fatigue than frequency domain based decompositions. Furthermore, the proposed method works under non-stationary conditions, e.g. under rapid angular acceleration and during transient motions. By exploiting the spatial deployment of sensors, the proposed transformation can produce information about the deformations in the body-fixed or material coordinates which is essential for stress analysis. The main feature of the method is the ability to separate modes of vibration that normally overlap in the frequency domain, to enable better insight into the sources of vibration. The method is demonstrated by analytical, numerical and experimental examples.

1. Introduction

Rotating disk vibrations can be described as a combination of alternating mechanical deformation-waves traveling relative to the disk itself or relative to a stationary frame [1–4]. These traveling waves change their behavior and their frequency contents with speed of rotation and through complex coupling effects and geometrical imperfections [5–7]. Turbines, compressors and computer disk-drives can all develop traveling vibration waves by virtue of their cyclo-symmetric geometry and because of their rotation relative to dynamic forces acting on the disk [3]. The complex nature of disk dynamics and the need for non-contacting measurement techniques has created several methods to extract the amplitude and phase of the individual modes of vibration. Many industries treat only synchronous vibrations using tracking filters [8] and tip-timing techniques (e.g. [9]). Other methods use a scanning laser sensor that continuously measures various sites on the rotating disk and with a parametric model the influence of individual modes can be estimated [10,11]. But, these methods can accommodate only constant speed of rotation and neither acceleration nor transients can be analyzed with this methodology in a satisfactory manner. Accelerating systems can develop non-synchronous vibrations during speed run-up due to the excitation of certain natural modes of vibration. The evolution of amplitude with speed and frequency has been treated in the past with a signal processing tool called Zmod [13] or by computing the time–frequency distribution [15] of measured signals. The term Zmod has historical roots in the

* Tel.: +972 4 8293153; fax: +972 4 8295711.
E-mail address: bucher@technion.ac.il

0022-460X/$ - see front matter © 2010 Elsevier Ltd. All rights reserved.
doi:10.1016/j.jsv.2010.09.033

aero-engine industry because it used the z-axis rear connector on old oscilloscopes. This ancient technique has been replaced nowadays by methods providing similar information via digital signal processing approaches. Digital signal processing software, mostly employing the discrete Fourier transform (DFT), can produce waterfall display having the ability to separate forward and backward whirling shaft motions [12,13]. Expanding these ideas for the separation of multiple wavelengths, commonly found in disks, results in the Zmod-like time–frequency information [13–16] with the ability to separate different modes according to the number of modal diameters (i.e. wavelength) [13] and where negative frequencies symbolize waves traveling in an opposite direction to the disk rotation speed [14–17]. Unfortunately, the methods described in [13–16] provide averaged, frequency domain data, and vibration levels during rapid transients can thus be underestimated. Clearly, all the available methods to compute time–frequency distributions, whether based on the discrete Fourier transform, Wigner–Ville distribution or wavelet decomposition [13–16], suffer from limited resolution. There is some tradeoff between obtainable time, frequency and space domains resolutions and therefore these methods provide poor estimates of the real vibration amplitudes under changing speed conditions. Resorting to transient capable decompositions such as wavelets or empirical mode decomposition (EMD) [18], some information can be extracted, but these methods divide the non-stationary signal into band-limited simpler components and are thus not suitable for disk vibration analysis. These methods do not separate different modes of vibration and are therefore unnatural for analyzing disk dynamics unlike the spatial Fourier transform.

It is preferred to analyze measured data using both the temporal and spatial properties that take into account the natural modes according to their number of nodal diameters. Indeed, this separation is common practice in numerical and analytical methods of cyclic structures (see [19] for an example). Dynamics specialists often use numerical and analytical decomposition of the individual modes in order to assess dangerous operating regimes [20,1–7]. With this separation, it is easier to identify the most excited modes of vibration thus isolating the cause for the observed vibrations.

Rotating disk-like structures (e.g. jet engine bladed disks) exhibit complex vibrations in the sense that they contain a large number of frequencies attributed to shaft vibration, disk vibrations, a mixture of both and families of similar modes in bladed disks.

Despite the great effort that accompanies numerical modeling, measured data still provides the most accurate representation of the actual vibration pattern a rotating structure experiences. Indeed, experiments are carried out routinely at many manufacturing sites and laboratories, but most set-ups contain only one or two sensors per shaft section. While this arrangement is sufficient to understand shaft dynamics [21,22], more sensors are needed for rotating disk analysis. The importance of separating forward and backward shaft whirl motions has been well established in the past (e.g. [21,22]). Vibrating and rotating disk dynamics require a more elaborate approach (e.g. [10,11]) or larger number of sensors to decompose the vibrations, as has been shown before [13].

The present paper expands the method in [13] to the time domain thus allowing the test-engineer to obtain instantaneous data rather than an averaged one, in frequency domain.

Disk vibrations can be described by a combination of several deformations each having a different wavelength and which travel in the co- and counter-rotating direction of the disk [1–7]. Each wavelength propagates at a different speed and therefore signals from stationary sensors, mounted on the foundation, cannot be used directly to estimate the stress on rotating parts.

The proposed method uses an array of sensors that allows one to separate the individual components in the time/amplitude, wavelength and direction senses to be later re-combined in the body-fixed coordinates.

Often, the speed of rotation and hence the vibration patterns are not stationary and thus the measured response is no longer composed of aggregates of sinusoidal components. Non-stationary signals do not lend themselves well to decomposition in terms of amplitudes frequencies and phases [23]. Thus, a combination of traveling vibration waves having multitude of wavelengths and time-varying frequencies and which travel at different speeds, cannot be separated by conventional frequency-domain (Fourier) analysis or even with commonly used tracking filters [8]. The ability to decompose the traveling waves into their basic components is important for the understanding of the underlying physical phenomena (see [20]) and for the accurate assessment of stress levels. The present paper makes use of spatial and temporal information, that an array of sensors provides, to decompose and project the traveling waves onto the moving (rotating) material and thus producing information about what each material point senses. The Hilbert [23–25] and spatial Fourier transforms are combined here to generate time domain components that carry all the relevant information. A similar analysis that exploits frequency domain data [13], inevitably used averaging, and therefore could not produce correct estimates of the maximal stress levels. For these reasons, the proposed decomposition could be useful in fatigue and failure prevention studies.

The paper begins with a mathematical background and derivation of the method from an analytical perspective. Section 3 describes a numerical implementation of the method and finally Section 4 demonstrates the proposed method on experimentally obtained data and explains the meaning of some results.

2. Decomposition of sensor array signals in rotating machines

Consider a circular array of sensors mounted above a rotating disk as shown in Fig. 1. Being cyclically symmetric, the response measured at a fixed radius r_0 is a spatially periodic function of the angle of rotation denoted here as, θ. Assuming

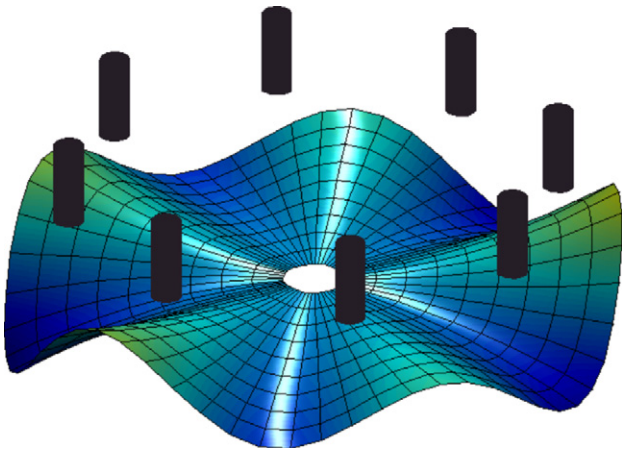

Fig. 1. Deformed rotating disk and a stationary array of sensors.

the rotating disk operates under time varying conditions, its response, as measured by a sensor located at the polar coordinate –(r_0,θ), can be expressed as

$$s(\theta,t)=\sum_{n=0}^{\infty} a_n(t)\cos n\theta+b_n(t)\sin n\theta,\quad \theta\in[0,2\pi] \tag{1}$$

Eq. (1) does not assume constant speed of rotation and therefore $a_n(t)$, $b_n(t)$ are general functions of time. In what follows, it is not necessary to assume that $a_n(t)$,$b_n(t)$ have meaningful instantaneous amplitude and phase (see [18,23]). Instead, it is assumed that they are a summation of some unknown functions that do have meaningful instantaneous amplitude and phase (individually) (see [23–25,18] for definitions). In order to simulate such functions, these coefficients are expressed here as a combination of real functions whose instantaneous amplitudes ($\alpha_r(t)$, $\beta_r(t)$) and phases ($\phi_r(t)$, $\vartheta_r(t)$) change with time

$$a_n(t)=\mathrm{Re}\sum_{n=0}^{\infty}\alpha_r(t)e^{i\varphi_r(t)},\quad b_n(t)=\mathrm{Re}\sum_{n=0}^{\infty}\beta_r(t)e^{i\vartheta_r(t)} \tag{2}$$

Substituting Eq. (2) in Eq. (1), one obtains

$$s(\theta,t)=\frac{1}{2}\mathrm{Re}\sum_{n}\sum_{r}\alpha_r(t)(e^{i(\varphi_r(t)+n\theta)}+e^{i(\vartheta_r(t)-n\theta)})-i\beta\alpha_r(t)(e^{i(\varphi_r(t)+n\theta)}-e^{i(\vartheta_r(t)-n\theta)}) \tag{3}$$

This expression is composed of complex exponentials, where $e^{i(\varphi_r(t)+n\theta)}$,$e^{i(\vartheta_r(t)-n\theta)}$, represent forward and backward traveling waves, respectively (see [1,3,15]). The 'Re' operator projects the result onto the real axis.

Clearly $a_n(t)$ and $b_n(t)$ carry the same information as the instantaneous amplitudes and phases. Having obtained $a_n(t)$ and $b_n(t)$, one can separate the deformation of the nth nodal diameter related response into forward and backward progressing patterns. Indeed, the phase as well as the amplitude can be approximated at every frequency by employing a time–frequency decomposition of $a_n(t)$ and $b_n(t)$ [13,15]. This transformation cannot be employed in real time nor can it be used to produce accurate time domain data (only an averaged version thereof). For this reason, the relative phase is obtained in this paper by means of the Hilbert transform. Applying the Hilbert transform (denoted by $H[\,\cdot\,]$) to Eq.(1), the analytic signal is obtained [18,23–25]:

$$\hat{s}(\theta,t)=\sum_{n=0}^{\infty}\hat{a}_n(t)\cos n\theta+\hat{b}_n(t)\sin n\theta \tag{4}$$

Here $\hat{f}(t)\triangleq f(t)+iH[f(t)]$ and $f(t)\in\{s,a,b\}$.

Using Euler's identity and dropping the explicit time dependency for brevity, Eq. (4) can be expressed as

$$\hat{s}(\theta,t)=\sum_{n=0}^{\infty}c_n^{+}e^{in\theta}+c_n^{-}e^{-in\theta}=\sum_{n=-\infty}^{\infty}c_n e^{in\theta} \tag{5}$$

where $c_n^{\pm}(t)\equiv c_n^{\pm}\triangleq(\hat{a}_n\mp i\hat{b}_n)$ and $c_n\triangleq\begin{cases}c_n^{+}, & n\geq 0\\ c_n^{-}, & n<0\end{cases}$,

Given the Hilbert transformed measured response, $\hat{s}(\theta,t)$, these time-dependent coefficients can be retrieved by performing integration (see [1]):

$$c_m = \frac{1}{2\pi}\int_0^{2\pi} \hat{s}(\theta,t)e^{-im\theta}\,\mathrm{d}\theta, \quad m=-\infty\cdots\infty \tag{6}$$

Clearly, it is unrealistic to assume that the response can be measured at any circumferential angle as required by Eq. (6). This requirement will be relaxed later on and is being used in this part solely for analytical development and demonstration.

It is worth mentioning that since $\hat{s}(\theta,t)$ is complex, $c_m \neq \overline{c}_{-m}$ (not complex conjugate pairs) as would be in the case of a real function. Indeed, $c_n^+ = c_n^+(t) = c_{n\geq 0}$ stands for the instantaneous complex amplitude of the forward (or co-rotating) traveling nth nodal diameter mode [1–7,10,13]. The second set of functions, $c_n^-(t) = c_{n<0}$ serves the same role for the backward traveling waves (counter-rotating) as $c_n^+ = c_n^+(t) = c_{n\geq 0}$ for forward traveling ones.

2.1. An analytical example

The proposed decomposition method is now demonstrated by considering two traveling waves having time-varying amplitudes. It is assumed, that the angle, θ, is a continuous variable, an assumption that will be dropped later on. Define the measured response in this example, as

$$s(\theta,t) = A_+(t)\cos(\omega t - n\theta) + A_-(t)\cos(\omega t + n\theta), \quad \theta\in[0,2\pi] \tag{7}$$

where it is assumed that $A_+(t), A_-(t)$ and $\cos(\omega t \mp n\theta)$ have non-overlapping spectra according to [24]. And $A_+(t), A_-(t)$ both have slower dynamics than $\cos(\omega t \mp n\theta)$ [23,24].

Using trigonometric identities, Eq. (7) can be expanded into

$$s(\theta,t) = A_+(t)(\cos\omega t\cos n\theta + \sin\omega t\sin n\theta) + A_-(t)(\cos\omega t\cos n\theta - \sin\omega t\sin n\theta) \tag{8}$$

Now, applying the Hilbert transform to Eq. (7), one obtains [23–25]:

$$H[s(\theta,t)] = A_+(t)\sin(\omega t - n\theta) + A_-(t)\sin(\omega t + n\theta) \tag{9}$$

The analytic signal can now be expressed by combining Eqs. (7) and (9):

$$\hat{s}(\theta,t) = s(\theta,t) + iH[s(\theta,t)] = A_+(t)e^{i(\omega t + n\theta)} + A_-(t)e^{i(\omega t - n\theta)} \tag{10}$$

It will be demonstrated now why standard envelope and instantaneous frequency analysis provides useless information in the case of a multi-component signals. Later, it will be shown how the exploitation of spatial data separates different waves yielding the required simplification.

Having obtained Eq. (10), the instantaneous amplitude and frequency can be computed via

$$\left|\hat{s}(\theta,t)\right|^2 = A_+^2(t) + A_-^2(t) + 2A_+(t)A_-(t)\cos 2n\theta \tag{11}$$

The instantaneous phase, which is computed below [23], becomes too complicated an expression to provide any useful interpretation:

$$\dot{\phi}(\theta,t) = \frac{\mathrm{d}}{\mathrm{d}t}\arctan\frac{\mathrm{Im}\left(\hat{s}(\theta,t)\right)}{\mathrm{Re}\left(\hat{s}(\theta,t)\right)} = \frac{\mathrm{d}}{\mathrm{d}t}\arctan\frac{A_+(t)\sin(\omega t + n\theta) + A_-(t)\sin(\omega t - n\theta)}{A_+(t)\cos(\omega t + n\theta) + A_-(t)\cos(\omega t - n\theta)} \tag{12}$$

But, once we employ the decomposition, as suggested in Eqs. (4)–(6), the two waves are separated, i.e.

$$\frac{1}{2\pi}\int_0^{2\pi}\hat{s}(\theta,t)e^{-in\theta}\,\mathrm{d}\theta = A_+(t)e^{i\omega t}, \quad \frac{1}{2\pi}\int_0^{2\pi}\hat{s}(\theta,t)e^{in\theta}\,\mathrm{d}\theta = A_-(t)e^{i\omega t} \tag{13}$$

It was shown that via the two stage process: (i) converting the response to an analytic signal and (ii) separating individual waves by means of spatial integration, the amplitude and phase of every component (and thus the instantaneous frequency) can be retrieved. Here, the complex functions $A_+(t)$, $A_-(t)$ represent the forward and backward traveling response in the *time domain*. These were found by means of a spatial Fourier transform (Eq. (6)). It is worth reminding that both $A_+(t), A_-(t)$ have time-varying amplitudes and thus may contain many frequencies and can in fact be non-stationary signals. Eq. (13) contains meaningful time domain data that can be used to compute the instantaneous amplitudes and phases alongside with the evolution of its spectra.

3. Practical implementation of the decomposition method

In the previous example, the analysis was carried out assuming that the sensors are continuously distributed along the circumference. In reality, sensors can be placed on the structure only at discrete locations.

Consider the discrete Fourier transform of N signals coming from N sensors, distributed at a uniform angular spacing of $2\pi/N$ (rad). Uniform spacing in the entire range guarantees exact results, completely identical to Eq. (6) with no need to apply a spectral window [27]. It is important to stress that no numerical approximation is involved in this part.

The kth coefficient (time function) can be computed exactly via Eq. (14) in a completely analogous manner to Eq. (6), as long as N is large enough to rule out spatial aliasing [1,15,27]:

$$S_k(t) = \sum_{n=0}^{N-1} s_n(t) e^{-i(2\pi kn)/N} = \sum_{n=0}^{N-1} s_n(t) \cos\frac{2\pi kn}{N} - i s_n(t) \sin\frac{2\pi kn}{N} \tag{14}$$

Now computing the analytic signal of Eq. (14) as before, one has

$$\hat{S}_k(t) = \sum_{n=0}^{N-1} \hat{s}_n(t) \cos\frac{2\pi}{N} kn - \mathrm{i}\hat{s}_n(t) \sin\frac{2\pi}{N} kn \tag{15}$$

where

$$\hat{S}_k(t) = S_k(t) + iH[S_k(t)] \triangleq S_k(t) + iG_k(t) \tag{16}$$

The Hilbert Transform of each measured sensor is denoted

$$g_k(t) \triangleq H[s_k(t)], \quad k = 0,\ldots,N-1 \tag{17}$$

One can now obtain an explicit expression for the analytic signal of the kth wavelength:

$$\hat{S}_k(t) = \sum_{n=0}^{N-1} (s_n(t) + \mathrm{i}g_n(t)) \cos\frac{2\pi kn}{N} - \mathrm{i}(s_n(t) - \mathrm{i}g_n(t)) \sin\frac{2\pi kn}{N} \tag{18}$$

Separating real and imaginary, one finally obtains

$$\begin{aligned} p_k^R(t) &\triangleq \mathrm{Re}\,\hat{S}_k(t) = \sum_{n=0}^{N-1} s_n(t) \cos\frac{2\pi kn}{N} + g_n(t) \sin\frac{2\pi kn}{N} \\ p_k^I(t) &\triangleq \mathrm{Im}\,\hat{S}_k(t) = \sum_{n=0}^{N-1} g_n(t) \cos\frac{2\pi kn}{N} - s_n(t) \sin\frac{2\pi kn}{N} \end{aligned} \tag{19}$$

It is worth mentioning that the negative ongoing vibration waves are obtained for $k > (N/2)$, i.e.

$$p_k(t) \equiv p_{k-N}(t) \triangleq p_{-k}(t), \ \forall k > \frac{N}{2} \tag{20}$$

The wave components are inevitably complex functions of time thus carrying both amplitude and phase information at any moment in time:

$$p_n(t) \triangleq p_n^R(t) + ip_n^I(t) \tag{21}$$

Eq. (19) is the result of both a Hilbert and a subsequent spatial Fourier transform. The process produces time functions representing the instantaneous variation of the nth nodal diameter modes traveling in either the positive or negative direction.

The number of sensors—N should be chosen according the shortest wavelength (i.e. the largest number of nodal diameters) one expects to be excited in the frequency range of interest [13,27]. Assuming that $n_{\max}$ is the largest number of nodal diameters present in the response, one should place at least $N=2n_{\max}$ sensors spaced $2\pi/N$ (rad) apart at some constant radial distance in order to avoid spatial aliasing.

3.1. A numerical example

Consider a rotating disk whose dynamics are measured by $N=16$ equispaced sensors. The simulated measurements for each one of the 16 sensors are computed via:

$$s(\theta,t) = \mathrm{Re} \sum_n \sum_r \alpha_r e^{i\omega_c t} e^{\mathrm{i}(\varphi_r(t) + n\theta)}, \quad s_k(t) = s(\theta,t)\big|_{\theta = 2\pi k/16}, \quad k = 0,\ldots,15 \tag{22}$$

The instantaneous phase of each component, representing either run-up or run-down of the rotating system, is computed by

$$\varphi_r(t) = \omega_r + \gamma_1 t + \gamma_2 t^2, \quad \varphi_r(0) = \varphi_0 \tag{23}$$

and the instantaneous amplitude, as can be seen in Eq. (2), is $\alpha_r\, e_c^{t\omega}$. The set of parameters that was used in the simulation is provided in Table 1.

The simulation uses a sensor array similar to the one in Fig. 1, the simulated response at one of the sensors is shown in Fig. 2. Clearly the signal, being composed of several non-synchronous and non-stationary components, looks rather erratic. Employing a time–frequency transformation (short-time Fourier transform (STFT) [15]), the true nature of the signal is better understood and the evolution of the various slowly varying components with time can be visualized in Fig. 3. The STFT uses a sliding window (see [13,15]) thus imposing certain averaging and therefore the maximal amplitudes can be greatly underestimated. Fig. 3 shows a qualitatively realistic case thus demonstrating the difficulty one may encounter when attempting to relate the measured response to individual modes of vibration at some speeds of rotation. The various components overlap (e.g. around time 0.5 and frequency 0.5 in Fig. 3) to a degree it would be impossible to tell which mode is dominant. The proposed decomposition attempts to unravel the hidden information.

Finally, the proposed algorithm is employed with the 16 measured sensors via Eq. (19). The real part of the decomposed signals is depicted in Fig. 4 showing in great detail that the individual components are considerably simpler than the raw signal. The standing ($n=0$), the forward traveling components ($n=1,\ldots,5$) and the backward traveling waves ($n=-1,\ -2,\ -3,\ -4$) have been successfully separated. In order to illustrate that the components have been separated, the components for $n=-3$ and 3 have been transformed via the STFT and are shown in Figs. 5 and 6. It is clear that the forward component (Fig. 5) contains a single time-varying frequency while the backward part in Fig. 6 eliminated all the other wavelengths to detect the crossing of an up-going frequency with a down-going one.

3.2. Projecting the stationary response to body-fixed coordinates

Although the decomposition provides a significant simplification of the raw measurements, the information that really matters, from a strength of materials perspective, is the deformations the disk material experiences.

The disk whose dynamics we wish to analyze is rotating at a variable speed, $\Omega(t)$, relative to the (inertial) circular array of sensors. It has been shown (e.g. [1,15]) that the inertial sensor array can be rotated virtually to an equivalent array that

Table 1
Coefficients of the simulated disk measured data used in Eqs. (2) and (3).

Name	r	n	ω_r	γ_1	γ_2	α_r	ω_c	φ_0
Mode 0	0	0	ω_r	3	3	0.2	2.1	0
EO 1	1	1	0	13.96	0	0.2	0.01	0
EO 2	2	2	0	27.93	0	0.16	0.013	0
EO 3	3	−3	0	41.89	0	0.24	0.03	0
Mode 1f	4	1	160	3	−0.05	0.23	0.1	0
Mode 1b	5	−1	160	−3	0.05	0.15	0.13	0
Mode 2f	6	2	260	6	−0.0667	0.26	0.31	−0.6
Mode 2b	7	−2	260	−6	0.0667	0.32	0.52	0.6
Mode 3f	8	3	760	12	−0.2	0.47	0.111	−0.31
Mode 3b	9	−3	760	−12	0.2	0.3	0.21	0.1
Mode 4f	10	4	1760	18	−0.1	0.3	1.2	−0.231
Mode 3b	11	−4	1760	−18	0.1	0.23	1	0.41

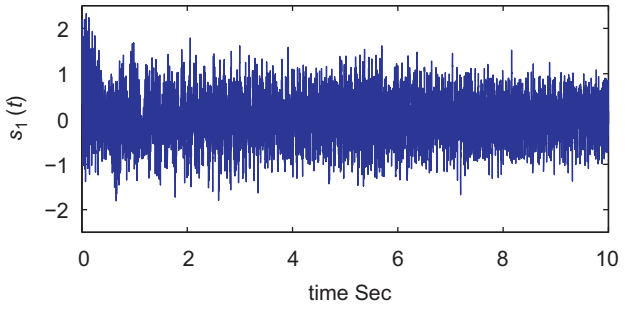

Fig. 2. A simulated measurement from sensors from $s_1(t)$.

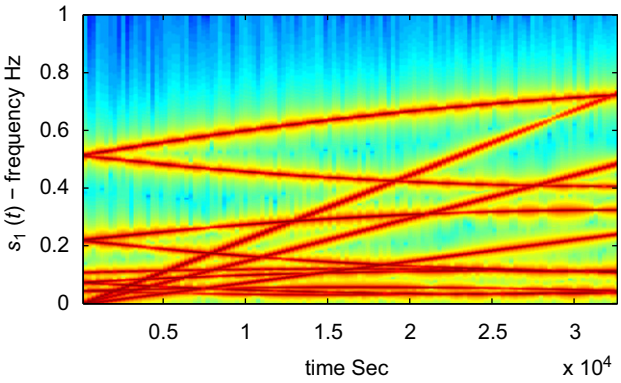

Fig. 3. Time–frequency distribution (STFT) of the simulated rotor using $s_1(t)$.

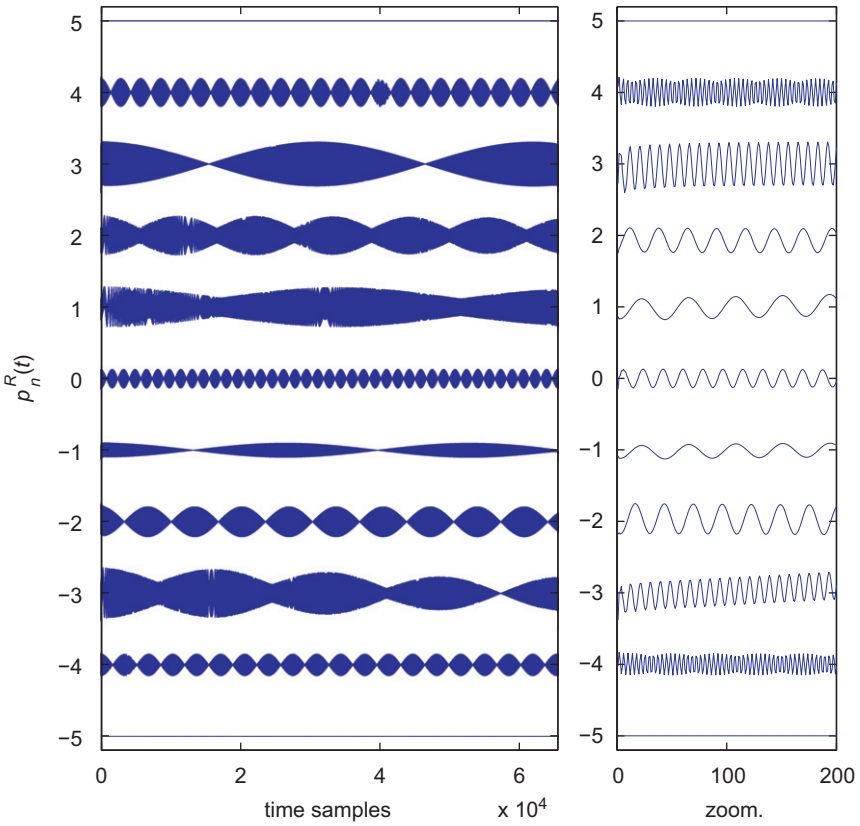

Fig. 4. Left: Decomposed time signals for example in Section 3.1 and right: zoomed fraction.

follows the material points on the rotating disk via the transformation:

$$(r_0,\theta)\rightarrow\left(r_0,\theta+\int\Omega(t)\,\mathrm{d}t\right) \tag{24}$$

Denoting $\phi=\theta+\int\Omega(t)\,\mathrm{d}t$, one can substitute $\theta=\phi-\int\Omega(t)\,\mathrm{d}t$ in Eq. (3) to obtain the information that would have been provided by a sensor placed at (r_0,ϕ) relative to a coordinate system attached to the rotating disk. In body fixed coordinates, one would measure:

$${}_b\hat{s}(\phi,t)=\sum_{n=0}^{\infty}c_n^+(t)e^{in(\phi-\int\Omega(t)\,\mathrm{d}t)}+c_n^-(t)e^{-in(\phi-\int\Omega(t)\,\mathrm{d}t)} \tag{25}$$

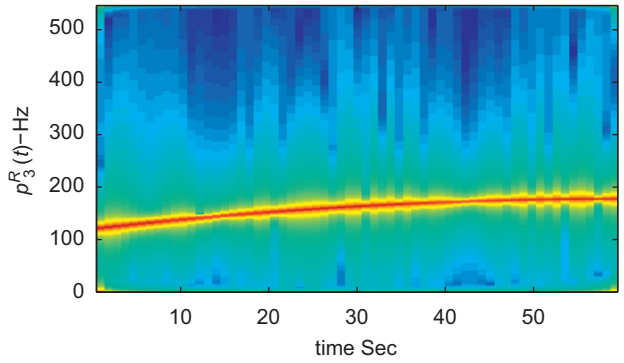

Fig. 5. Real part of decomposed component $p_3^R(t)$ example in Section 3.1.

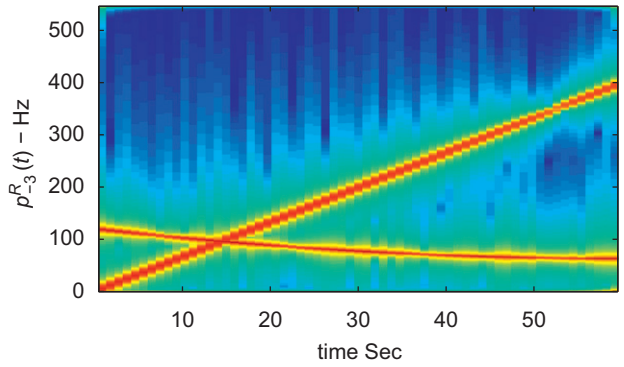

Fig. 6. Real part of decomposed component $p_{-3}^R(t)$ example in Section 3.1.

Simplifying,

$$ {}_b\hat{s}(\phi,t) = \sum_{n=0}^{\infty} c_n^+(t) e^{-in\int \Omega(t)\,\mathrm{d}t} e^{in\phi} + c_n^-(t) e^{+in\int \Omega(t)\,\mathrm{d}t} e^{-in\phi} \tag{26} $$

The instantaneous phase is typically measured by an encoder or a resolver (see [1,8,15]), as was done in the experiments described later on.

Indeed, the instantaneous phase of the rotating part is defined via

$$ \Psi(t) = \int_0^t \Omega(\tau)\,\mathrm{d}\tau \tag{27} $$

which can be measured in practice using a shaft-encoder or a resolver.

Having obtained $c_n^{\pm}(t)$ (from Eq.(6) or its discrete counterpart via Eq.(19)), one can estimate $\hat{s}(\phi,t)$. Individually decomposed waves of vibration can be transformed to the body-fixed coordinate system, via

$$ {}_bc_n^+(t) = c_n^+(t) e^{-in\Psi(t)} \tag{28} $$

where ${}_bc_n^+(t)$ serves the same role as $c_n^+(t)$ but in the body fixed frame of reference. In the discrete case, where an array of sensors is being used, the notation:

$$ {}_bp_n^+(t) = p_n^+(t) e^{-in\Psi(t)} \tag{29} $$

is adopted.

The transformation presented here can be used to project data from any pair of relatively rotating frames of reference and is not limited to produce body-fixed information from stationary sensors. For example, it may be desired to project data measured on a rotating disk (i.e. via strain gauges) onto another disk or engine casing to assess the deformation or forces in its own frame of reference. The same idea can be employed in these cases as long as the relative, instantaneous phase is available.

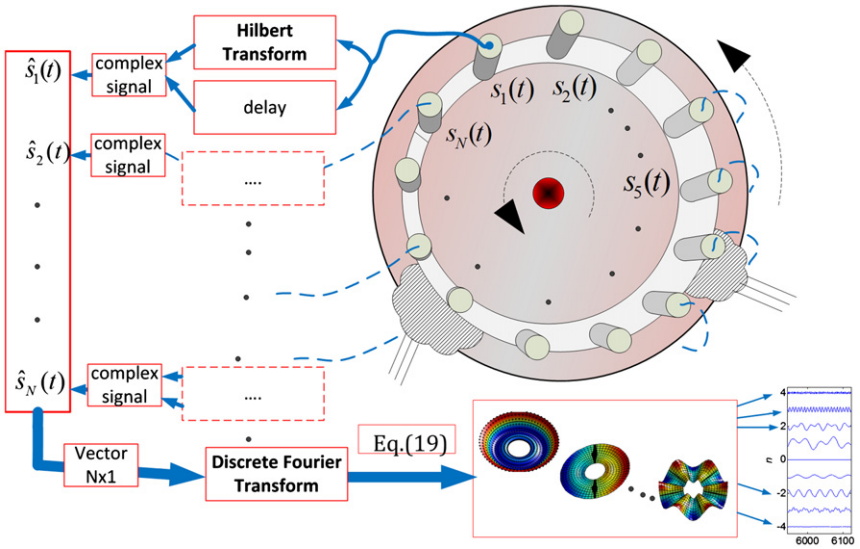

Fig. 7. Schematic description of data flow in the proposed decomposition.

3.3. *Data flow and the implementation of the algorithm*

The envisaged realization of the proposed method is pictorially described in Fig. 7. Inspecting this figure it is possible to identify the circular sensor array fixed to a stationary ring. Behind the sensors-ring resides a rotating disk whose vibration are measured by the system. The proposed algorithm can operate in two cases: (i) the first, which is shown here, treats the case where the vibrating disk rotates relative to the sensors and (ii) the measuring sensors are fixed to the rotating disk's frame of reference (e.g. strain gauges with telemetric wireless transmission). In both cases, the schematic description in Fig. 7 is identical. Every sensor is wired to a Hilbert transformer block (which can nowadays be implemented by a FPGA chip in real time [28]). The Hilbert transformed signal and a slightly delayed version of the original data are combined to form an analytics signal and fed into a discrete, spatial Fourier transformer that can also be programmed in a FPGA or a digital signal processor (DSP) [27]. The outcome of these computations provide instantaneous amplitude (and phase) data of the various modes, as shown graphically in Fig. 7. The algorithm generates the time functions shown at the end of the data chain in Fig. 7, but with the physical model, they can be interpreted by considering the level every mode, contributes to the measured response as illustrated by the deformed mode shapes representing the various modes in terms of the number of nodal diameters.

4. Experimental examples

In the previous example the analysis was carried out for a simulated signal representing the response of a disk with speed-dependent natural frequencies. The model incorporated several effects: natural frequency split due to gyroscopic coupling, centrifugal stiffening and softening modulation of the amplitude and frequency changes while speed was changing [1,2,4–6,27].

In this section, a laboratory test-rig (see Figs. 8 and 9) was used to provide data as explained below. The data was used in two decompositions:

(I) a simple forward and backward decomposition of the shaft whirl in the time domain making use of two sensors measuring the shaft bending and
(II) decomposition of the various disk modes with an array of N=8 sensors spread at equispaced angles along a flexible disk.

The experimental system, shown in Figs. 8 and 9 consisted of a 20 mm diameter flexible shaft, which was 1.0 m long. The shaft was mounted on two self-aligning ball-bearings and it was driven by a 20 N m rated AC brushless motor capable of running up to 4500 rev/min. A flexible disk was mounted on the other end of the shaft. In the middle of the shaft a virtual cross section through an active magnetic bearing is shown (Fig. 8). In the present test, the magnetic bearing produced a small, band-limited random force to enrich the measurements and simulate the effect of turbulence in real jet-engines. Not shown in Fig. 8 are the electromagnetic exciter driving the disk (that can be seen on the far side of Fig. 9) and the sensor array measuring the disk vibration. The shaft vibrations were measured by two sensors connected at a right angle as can be seen in Fig. 9. The electromagnet driving the flexible disk was fed by a DC biased random current to excite

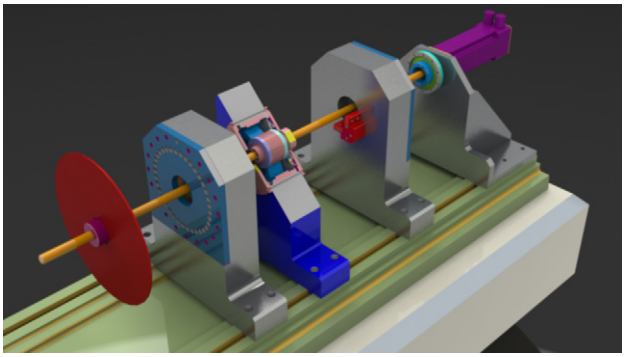

Fig. 8. Computer generated drawing of the experimental rig.

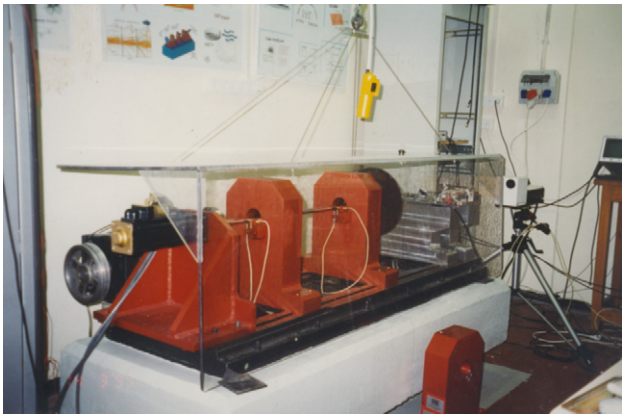

Fig. 9. Photograph of the experimental rig in the laboratory.

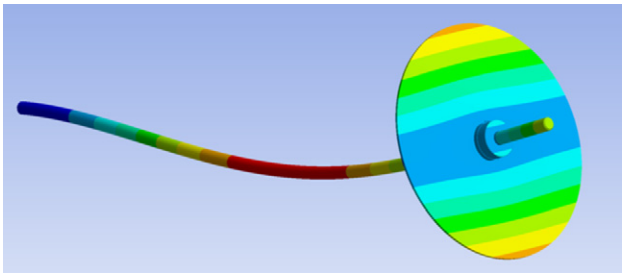

Fig. 10. Finite element generated mode shape showing shaft bending and $n=1$ disk mode.

the otherwise unexcited disk modes with more than two nodal diameters. During the experiment, the motor speed was brought up until it reached a predetermined upper limit, but the motor controller's gain was set to a low value so as to increase the interaction between the shaft vibration and the speed and create some speed fluctuations, as can be seen in Fig. 15. The fluctuations in speed are manifested in the deviation of the engine orders ($1\times$, $2\times$, etc.) from a straight line during the acceleration.

4.1. Real time shaft whirl decomposition

It is expected that disk modes having more than two nodal diameters would not be visible in the shaft bending vibrations, but those with one nodal diameter do involve shaft bending. By computing numerically (using Ansys^{TM}) the mode shapes of the system in Fig. 8, it is clear that Fig. 10 (exhibiting one disk nodal diameter) involves shaft bending while Fig. 11, showing a two nodal diameter disk modes, is completely decoupled from the shaft. There are two shaft bending modes in the frequency range excited by unbalance forces in this system. The large disk creates some gyroscopic split that separates the otherwise identical forward and backward whirling modes [21,22].

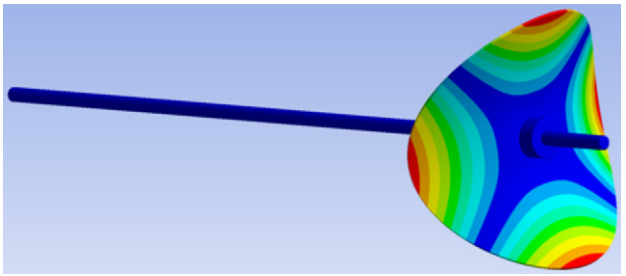

Fig. 11. Finite element generated mode shape showing n=2 disk mode.

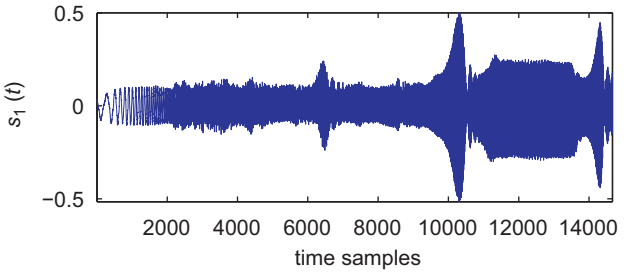

Fig. 12. Measured shaft vibrations using one of the sensors—$s_1(t)$.

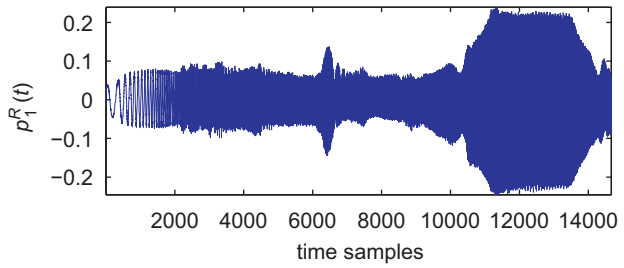

Fig. 13. Decomposed forward-whirling shaft vibrations—$p_1^R(t)$.

In the first example, two sensors, denoted s_1, s_2 (connected by the white cables seen in Fig. 9) measure the shaft bending vibrations in two orthogonal directions. The measured signals from the two sensors during a run-up, look nearly identical and the outcome of s_1 is shown in Fig. 12. There are several distinct peaks in this plot that are possibly attributed to critical speeds. This signal combines both the forward and the backward whirl frequencies that overlap almost completely in the frequency domain. It is known [21,22] that first engine order of the forward whirl creates no alternating stresses in this case (hence causing no fatigue) while the backward whirl creates oscillating stresses. The decomposition isolating the backward whirl part helps in examining the alternating stress which seems dangerous in the backward motion due to its twice per revolution alternating stress [21,22].

Since according to beam theory the shaft cross section remains undistorted, two sensors suffice to provide the necessary information that four sensors spaced 90° apart would provide [13]. Employing Eqs. (17) and (19), to the 4×1-vector $(s_1,s_2,-s_1,-s_2)$, Figs. 13 and 14 are obtained. The forward and the backward whirling part were obtained, much like what has been shown in the past (e.g. [12]), but here, the information is provided in the time domain. The rapid rise of the backward whirl in Fig. 14 when the frequency is close to the critical speed, indicates that the bearing stiffness is not isotropic [22]. This kind of behavior is a sensitive indicator for mechanical failures in the supports.

The obtained signals are non-stationary and therefore their spectral contents can be examined by means of a time–frequency distribution in order to validate the results while comparing to a previous work [13]. The time–frequency distribution of $p_n^R(t)$ (say) is denoted by $P_n^R(\omega,t)$ (see [15]). Fig. 13 is transformed into Fig. 15 and 14 into Fig. 16, in both cases the speeds and frequencies, where high response levels are obtained, can be clearly seen. It is clear that synchronous unbalance response is the most dominant component in the plot, and comparing Figs. 15 and 16 it can be seen that the forward and backward whirling branches of the natural modes were separated. The forward going branches tend to increase slightly with speed of rotation. The backward component shows the distinct effect of bearing anisotropy manifested by large backward (or reverse) whirl due to the forward rotating unbalance force. The reverse whirl related natural frequency tends to decrease slightly with speed as evident from Fig. 16.

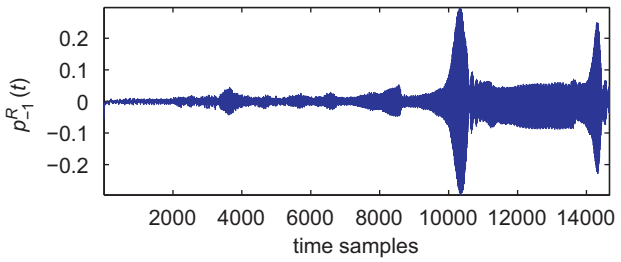

Fig. 14. Decomposed backward-whirling shaft vibrations—$p^R_{-1}(t)$.

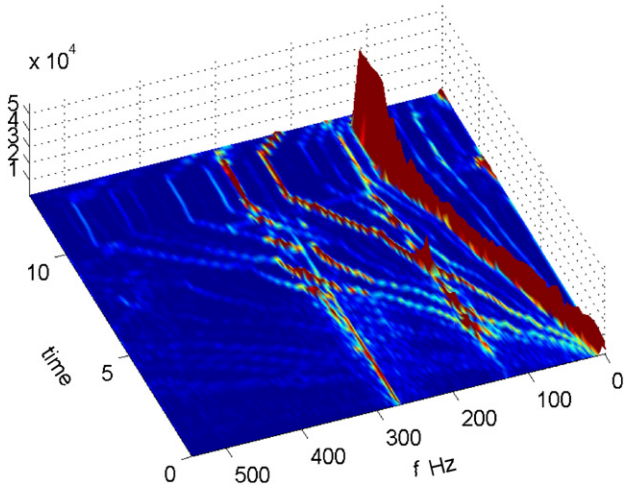

Fig. 15. Decomposed forward-whirling STFT—$P^R_1(\omega,t)$.

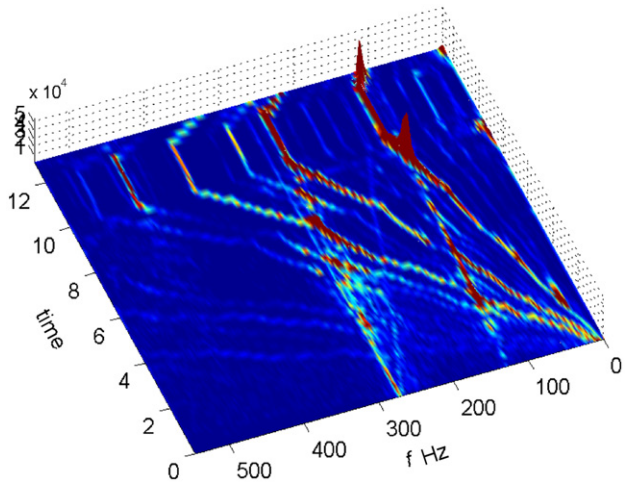

Fig. 16. Decomposed backward-whirling STFT—$P^R_{-1}(\omega,t)$.

By inspecting the slope of the natural frequency lines it was proven that indeed the forward and backward components have been isolated by Eq. (19). Furthermore, the separation of these components in the time domain allows one to accurately assess the vibration level of each component. The forward whirl seems to be highly effected by shaft run-out, judging from the large forward component at low speeds where unbalance has negligible effect. When subtracting the run-out from the forward whirl part, it is clear (even if somewhat surprising) that the backward component shows larger net vibration levels.

4.2. Real time experimental disk response decomposition

In order to decompose the disk vibration, N=8 sensors were placed in a similar manner to what appears in Fig. 1. The disk in Figs. 8 and 9 was excited by an external electromagnetic, non-contacting device, that simulated external loading effects and the speed of rotation was changed during the measurement process. It is important to excite the disk in this case because the naturally occurring unbalance forces would not excite many of the disk modes, as evident from Fig. 11. In reality, these modes are excited by pressure fluctuations, in aero engines or due to magnetic forces in some machines.

Disk vibrations are expected to be richer than those measured on the shaft because of the additional modes that participate in the response. Disk modes may or may (Fig. 10) or may not Figs. 11 and 17 be affected by unbalance. Placing a single sensor to measure bending vibrations of the flexible disk, the response shown in Fig. 18 is obtained. Apart from minor peaks, it is difficult to notice anything unusual in this plot; therefore a time–frequency map was created with this signal and is shown in Fig. 19. In this figure, several engine orders alongside with shaft and disk related modes of vibration. Unfortunately, as can be noticed, all the information is condensed in the same frequency region which makes it is difficult

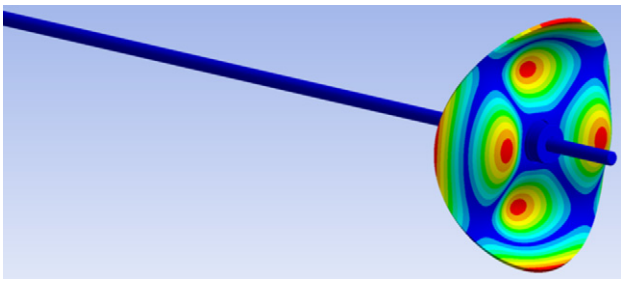

Fig. 17. Finite element generated mode shape showing n=2 disk mode with complex radial bending pattern.

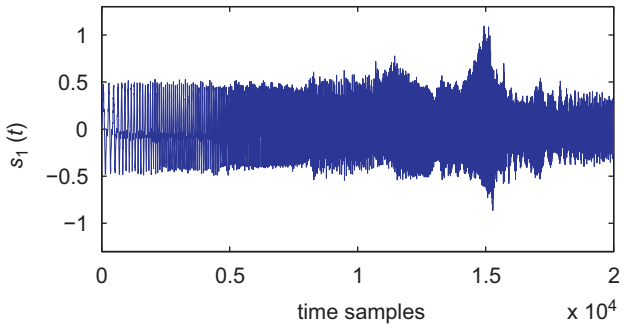

Fig. 18. Measured disk vibration from a single sensor—$s_1(t)$.

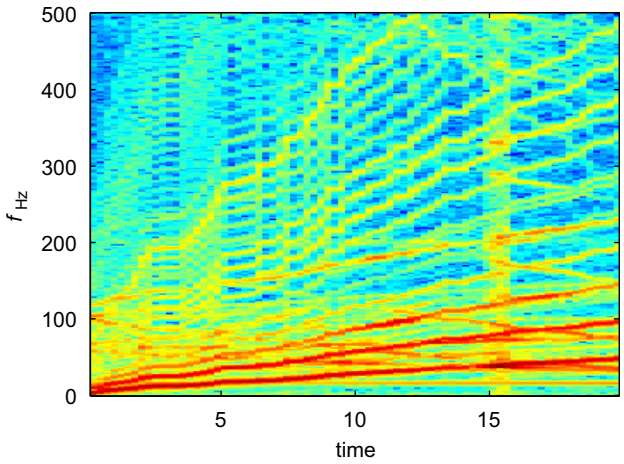

Fig. 19. STFT of measured data using a single sensor—$S_1(\omega,t)$.

to separate the components. Inspecting this figure it is clear that multiple crossing frequency lines exist which may cause severe difficulties in order-tracking based algorithms that are inferior when two frequencies are very close.

Having applied the proposed decomposition via Eq. (19), and which is illustrated in Fig. 7, the strength of each wavelength, either co-rotating or counter-rotating can be now clearly seen in Fig. 20. The positive (forward) going components ($p_n^R(t)$, $n>0$), show nearly constant amplitude while the speed of rotation was continuously raised. This can suggest that the displacement probes, used as sensors, actually measured the geometric imperfection of the disk with a small contribution due vibrations. On the backward progressing components, it can be seen (Fig. 20, $p_n^R(t)$, $n<0$) that for $n=-1,-2,-3$, peaks were observed at different instances of time suggesting that critical speeds or resonance conditions occurred. The right hand part of Fig. 20 isolates a short time fraction of the decomposed components in which is can be seen that the nature of these signals has clearly become simpler after performing the decomposition.

In order to illustrate the correctness of this decomposition, the individual components $p_n^R(t)$ (or $p_n^l(t)$ that carry similar information) can be used to produce a time–frequency distribution. Each component has a different time–frequency contents, as explained below.

The zeroth nodal diameter component ($n=0$) indicates circumferentially uniform motions of the disk (mushroom like modes). Two such flexible modes are visible in Fig. 21 where the largest one clearly shows centrifugal stiffening in Fig. 21

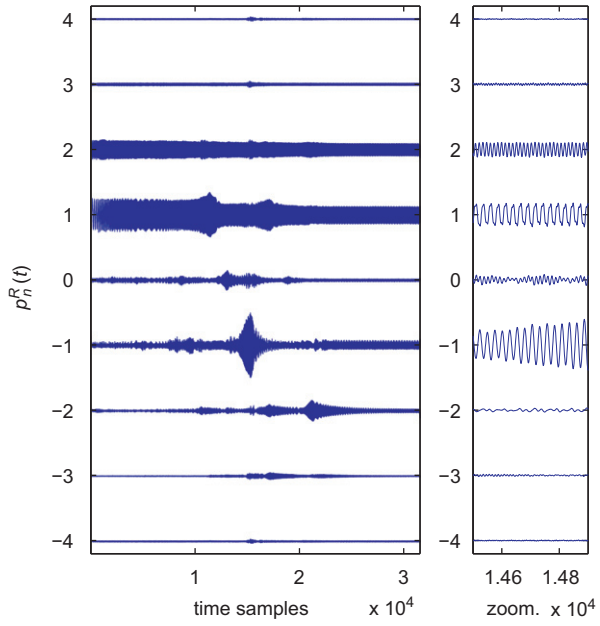

Fig. 20. Decomposed disk vibration for $n=-4\cdots4$—$p_n^R(\omega,t)$.

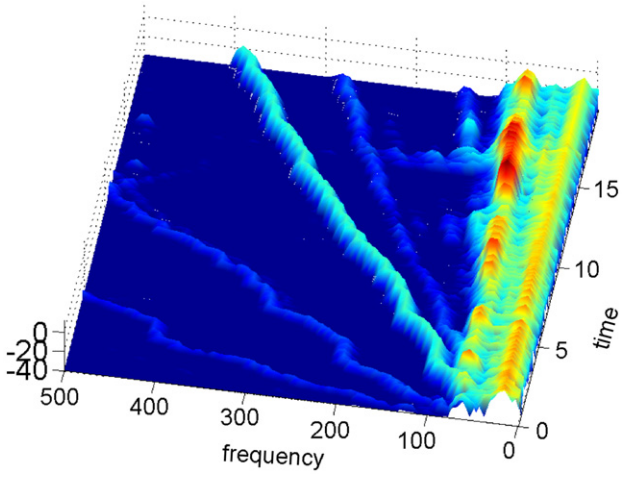

Fig. 21. STFT of decomposed $n=0$—$P_0^R(\omega,t)$.

(increase of the frequency of vibration vs. speed). Taking the one nodal diameter component, one can combine the information from $p^R_{+1}(t)$and $p^R_{-1}(t)$to create a forward–backward time–frequency map which is shown in Fig. 22, here positive frequency signifies forward traveling waves and negative frequency represents backward traveling ones. The negative-slope inclined line is caused by spatial aliasing but these components are much weaker than relevant ones, even in logarithmic scale. Clearly, the first engine order was isolated (compared with Fig. 19 where several engine orders are dominant) which demonstrates the separation achieved by Eq. (19). Here, in the forward part two components are dominant, one showing constant amplitude and is therefore only due to the static wobbliness of the disk and the second one, having a sharper increase in frequency is caused by unbalance. The backward component traces an increasing natural frequency (in the absolute sense, but it has a negative slope because it resides the negative frequencies part) with a peak at a backward whirl critical speed. Here too, some small amplitude, spatial aliasing is observed at higher frequencies.

Fig. 23 shows a line with a double slope compared with Fig. 22, due to the shorter wavelength attributed to n=2 (the frequency a fixed sensor measures due to a spatial sine with n nodal diameters is $n\Omega t$). The decrease in the frequency of the backward components is more noticeable than before, the forward, 2X engine order has nearly constant amplitude thus indicating that the proximity probes actually measured mostly the geometric (constant) distortion of the forward rotating disk.

Finally, for n=3, the same procedure yields Fig. 24. Apart from the more inclined engine order lines (3X), a disk critical speed is observed now in around 350 Hz. This could not have been easily detected without the decomposition. Another noticeable component is the resonating backward wave close to the highest speed. Since stress is related to the deformation the disk material senses, it is difficult to observe these facts in Fig. 19, but transforming the decomposition to the body-fixed coordinates reveals this fact, as explained below.

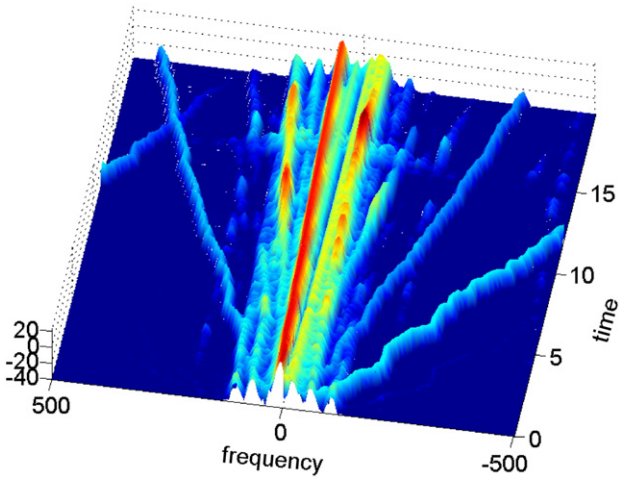

Fig. 22. Combined forward/backward STFT for $n=\pm1$—$P^R_{\pm1}(\omega,t)$.

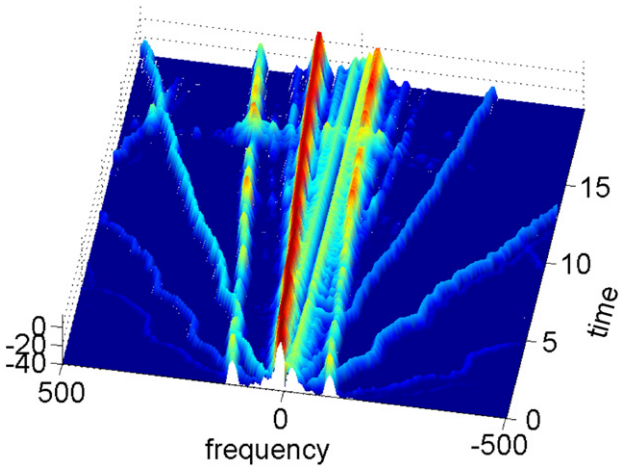

Fig. 23. Combined forward/backward STFT for $n=\pm2$—$P^R_{\pm2}(\omega,t)$.

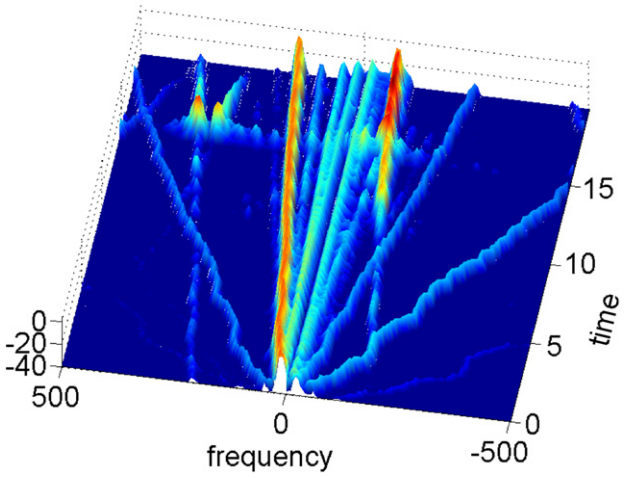

Fig. 24. Combined forward/backward STFT for $n=\pm 3$—$P^R_{\pm 3}(\omega,t)$.

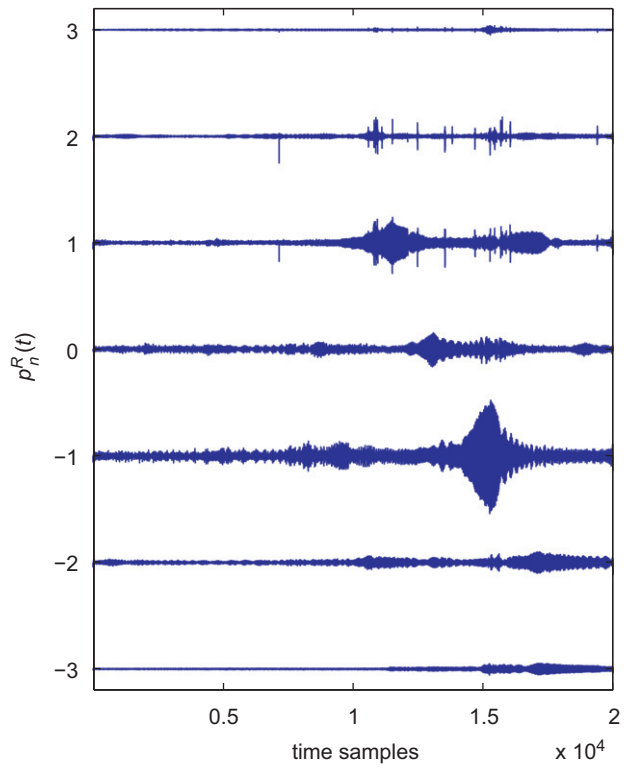

Fig. 25. Decomposed disk vibration transformed to body-fixed coordinates for—${}_b p^R_n(\omega,t)$.

4.3. *Transforming stationary to body-fixed measurements*

It has been suggested in the previous example that a significant part of the forward components is related to geometric imperfections and not to vibrations. The transformation to body fixed coordinates should eliminate these effects. In this part, the procedure in Section 3.2 was applied to the same data from the previous example. In addition to the N=8 measured signals, the instantaneous phase of the disk was measured. Applying Eqs. (19) and (28) to the measured data, the body fixed components, ${}_b p^{\pm}_n(t)$, n=1,2,3,…, are obtained and shown in Fig. 25. Indeed, Fig. 25 illustrates the elimination of the geometry imperfection attributed response. Disk imperfections do not oscillate in the body-fixed coordinates and are thus transformed to the zero frequency line. Forward and backward components have a totally different meaning than before because it is related here to waves traveling relative to the material points rather than relative to the sensor array. Inspecting Fig. 25 it is clear that the disk

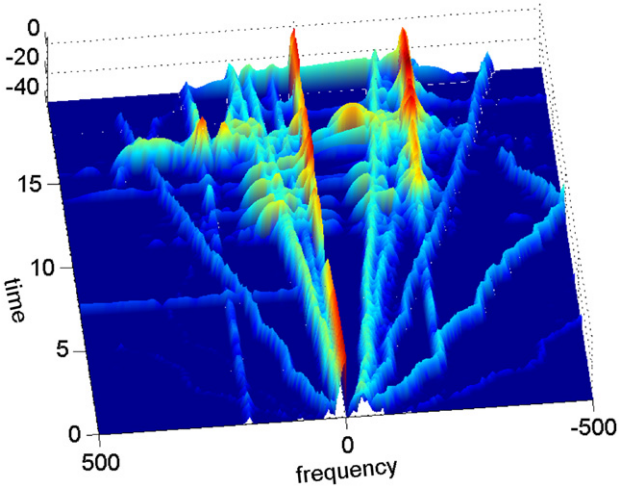

Fig. 26. STFT of decomposed components in body coordinates—${}_bP_n^R(\omega,t)$.

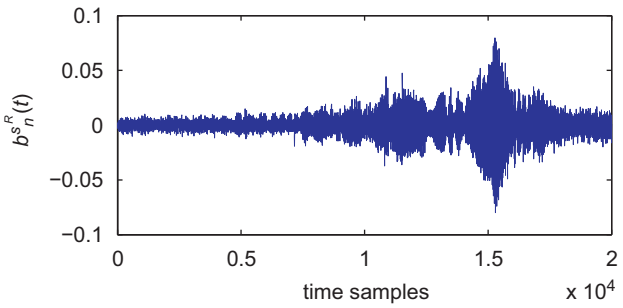

Fig. 27. Reconstructed virtual sensor measurement in body coordinates—${}_b\hat{s}((\pi/2),t)$.

vibration are in fact not as severe in the forward traveling part, as appeared in Fig. 20 which incorporated the effect of geometric imperfections. The largest component in the body-fixed coordinates is the $n=-1$ (backward) mode.

What is also revealing is the time–frequency distribution of the transformed components which show a significant contribution at zero frequency. When computing the STFT for ${}_bp_3^{\pm}(t)$ components (Fig. 26), a similar behavior is observed for other wavelengths too and once more, the geometric imperfections were transformed to zero frequency (middle line), i.e. fixed in the disk frame of reference. In the body fixed coordinates, both the forward and the backward traveling modes show an increase in frequency due to centrifugal stiffening. The same analysis, in the inertial coordinates, has resulted in a misleading frequency shift due to the Galilean transformation (see [1]).

Using Eq. (26), the true temporal response that the material experiences can be computed, despite the fact that a stationary sensor array has been used. Eq. (24) can be employed to create a signal such that a body-fixed sensor would measure. Specifically, a sensor fixed to the disk at 90°, would measure the signal appearing in Fig. 27 showing one of N time-response signals that can be retrieved by Eq. (24). The different components, each traveling at a different speed and direction, were correctly combined using the instantaneous measured phase $\Psi(t)$. The projected response is visibly different than what a fixed sensor (Fig. 18) measured.

The same procedure can be performed in real time by computing the Hilbert transform using a FIR recursive filter (see [26–28]) and by performing all the computations in real time using an embedded microprocessor.

5. Conclusion

A method to decompose and transform complicated vibration patterns that rotating disks experience was presented in this paper. The method uses an array of sensors to produce a time domain decomposition of the waves traveling in a rotating disk. By measuring the instantaneous phase of rotation, data measured by a stationary array of sensors can be projected onto the moving material. This projection can be performed only due to the separation into wavelengths, and into forward/backward travel direction.

As demonstrated in Section 4, the decomposition aids in separating shaft driven modes of vibration from disk affected ones. This is important information that can help the engineer in making judgmental decisions. For example, the large response observed at certain frequencies as shown in Figs. 23 and 24 is dominated by the $n=2,3$ (backward traveling wave). An attempt to dampen these vibrations with an active magnetic bearing acting on the shaft would be useless because these modes are decoupled from shaft bending (e.g. see Figs. 11 and 17). The method could also helps in diagnosing the cause for vibrations in certain cases by considering spatial fluctuations that contribute to certain modes. Excitation frequencies that stem from the kinematics of the machine, e.g. blade passing frequencies and gear meshing frequencies can possibly be indentified more clearly once the response has been separated into various components.

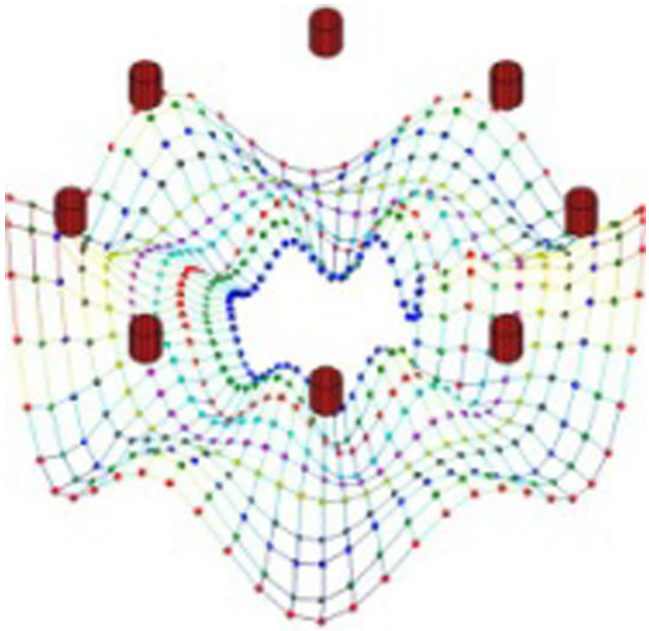

Video 1. Rotating disk undergoing steady-state vibrations containing several modes.

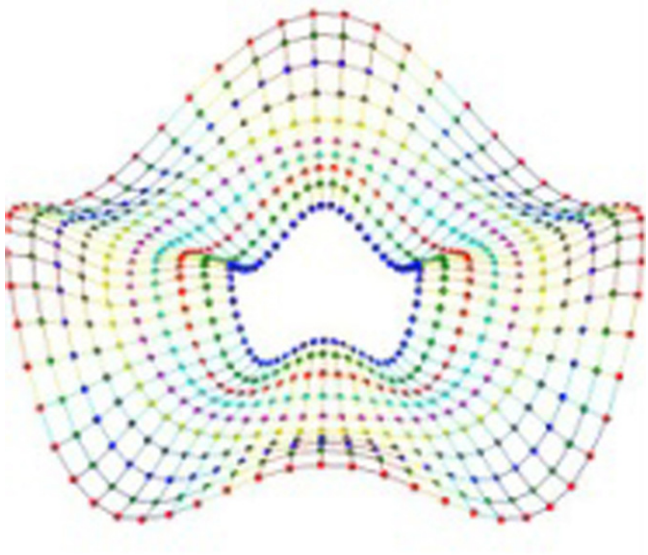

Video 2. $N=2$ nodal diameter wave traveling in opposite direction to rotation.

The method was demonstrated by means of a simple analytical example and by performing the decomposition on experimentally obtained data. The projection into body-fixed coordinates has created a more genuine view of the vibrating disks oscillatory motion removing misleading static geometric effects.

Supplemental material—multimedia videos

See Videos 1–6.

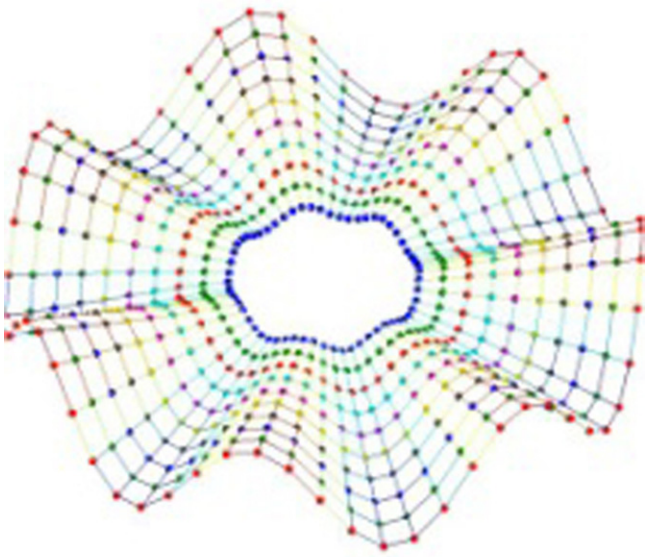

Video 3. Wave traveling in same direction as disk's rotation, fixed on disk.

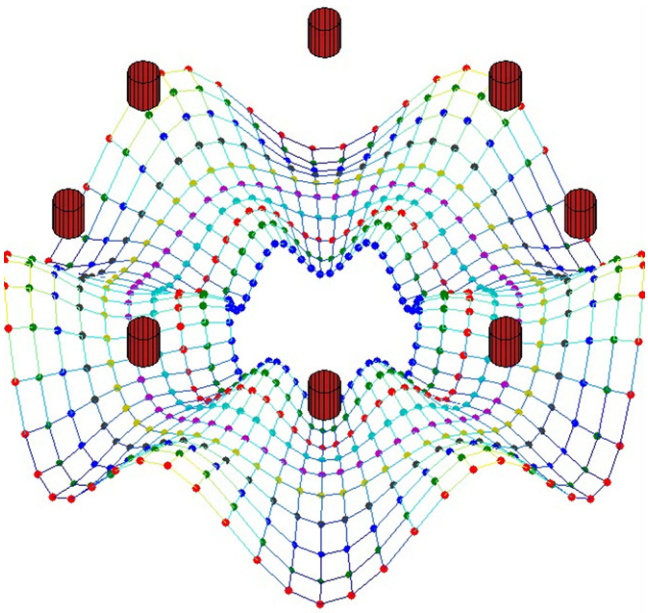

Video 4. Wave traveling in opposite direction to disk's rotation, fixed in inertial coordinates.

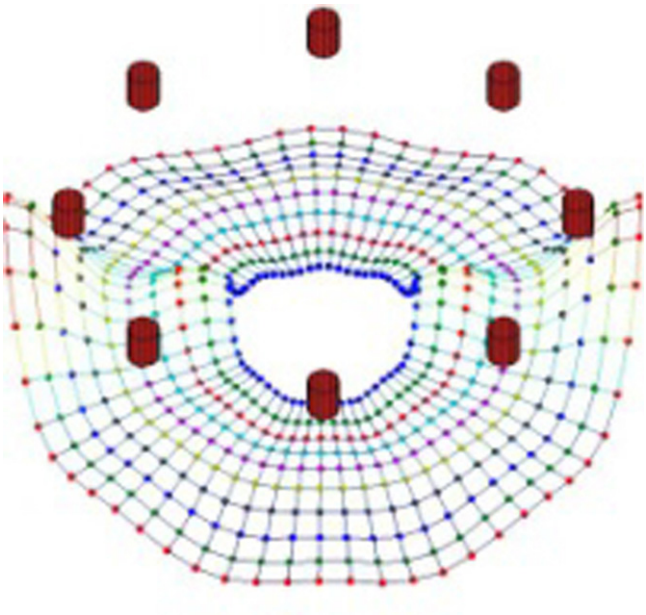

Video 5. Multiple wave traveling forward and backward during a transient while rotating.

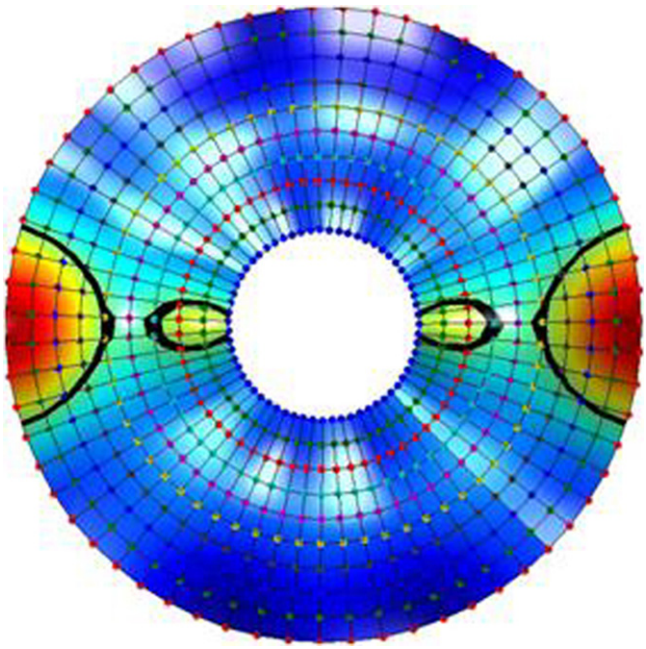

Video 6. Color-coded, multiple transient waves traveling forward and backward, illustrating the non-stationary position of nodal diameters.

References

[1] P. Schmiechen, Travelling-Wave-Speed Instability, PhD Thesis, Imperial College, London, UK, 1997.
[2] H. Lamb, R.V. Southwell, The vibrations of a spinning disk, *Proceedings of the Royal Society of London, Series A* 99 (699) (1921) 272–280.
[3] Y. Honda, H. Matsuhisa, S. Sato, Modal response of a disk to a moving concentrated harmonic force, *Journal of Sound and Vibration* 102 (4) (1985) 457–472.
[4] T.K. Ahn, C.D. Mote, Mode identification of a rotating disk, *Experimental Mechanics* 38 (4) (1998) 250–254.

[5] I.Y. Shen, C.D. Mote, Dynamic analysis of finite linear elastic solids containing small elastic imperfections: theory with application to asymmetric circular plates, *Journal of Sound and Vibration* 155 (1992) 443–465.
[6] S.A. Tobias, R.N. Arnold, The influence of dynamical imperfection on the vibration of rotating disks, *Proceedings of the Institute of Mechanical Engineers* 171 (1957) 669–690.
[7] S. Berger, E. Aubry, F. Marquet, G. Thomann, Experimental modal shape identification of a rotating asymmetric disk subjected to multiple-frequency excitation, use of finite impulse response fir1 filters, *Experimental Techniques* 27 (6) (2006) 44–48.
[8] H. Vold, J. Leuridan, High resolution order tracking at extreme slew rates, using Kalman tracking filter, SAE paper no. 931288, 1993.
[9] S. Heath, A new technique for identifying synchronous resonances using tip timing, *Journal of Engineering for Gas Turbines and Power* 122 (2000) 219–225.
[10] I. Bucher, P. Schmiechen, D.A. Robb, D.J. Ewins, A laser-based measurement system for measuring the vibration on rotating discs, *Proceedings of the International Conference on Vibration Measurement by Laser Techniques*, Ancona, Italy, October 1994, pp. 398–401.
[11] D. Di Maio, D.J. Ewins, Use of tracking-continuous scanning LDV (T-CSLDV) methods for vibration study of bladed disk assembly under operating conditions, *Proceedings of the 9th International Conference on Vibrations in Rotating Machinery*, Vol. 1, Exeter, UK, 2008, p. 317.
[12] A. Muszynska, Forward and backward precession of a vertical anisotropically supported rotor, *Journal of Sound and Vibration* 192 (1) (1996) 207–222.
[13] I. Bucher, D.J. Ewins, Multi-dimensional decomposition of time-varying vibration response signals in rotating machinery, *Mechanical Systems and Signal Processing* 11 (4) (1997) 577–601.
[14] Y.S. Han, C.-W. Lee, Directional Wigner distribution for order analysis in rotating/reciprocating machines, *Mechanical Systems and Signal Processing* 13 (5) (1999) 723–737.
[15] L. Cohen, *Time–frequency Analysis*, Prentice-Hall, Englewood Cliffs, 1995.
[16] M.-E.a Kim, C.-W. Lee, Use of dFRFs for identification of travelling wave modes in rotating disks, *Journal of Vibration and Acoustics, Transactions of the ASME* 120 (3) (1998) 719–726.
[17] I. Bucher, D. Ewins, Modal testing of rotating structures—a survey and some new results, *The Royal Society, Philosophical Transactions: Mathematical, Physical and Engineering Sciences* 359 (1778) (2001) 61–96.
[18] E. Norden Huang, S. Zheng, R.L. Steven, C.W. Manli, H.S. Hsing, Z. Quanan, Y. Nai-Chyuan, T. Chi Chao, H.L. Henry, The empirical mode decomposition and the Hilbert spectrum for nonlinear and non-stationary time series analysis, *Proceedings: Mathematical, Physical and Engineering Sciences* 454 (1971) (1998) 903–995.
[19] G. Genta, A Tonoli, A harmonic finite element for the analysis of flexural, torsional and axial rotordynamic behaviour of discs, *Journal of Sound and Vibration* 196 (1) (1996) 19–43.
[20] C.W. Lee, D.J. Han, Strength of modes in rotating machinery, *Journal of Sound and Vibration* 313 (1–2) (2008) 268–289.
[21] R. Gasch, R. Nordmann, *Rotordynamik*, 2nd ed, Springer, Berlin, 2007, in German.
[22] G. Genta, *Dynamics of Rotating Systems*, Springer, New York, 2005.
[23] S.L. Hahn, On the uniqueness of the definition of the amplitude and phase of the analytic signal, *Signal Processing* 83 (2003) 1815–1820.
[24] E. Bedrosian, A product theorem for Hilbert transforms, *Proceedings of the IEEE* 51 (1963) 68–89.
[25] M. Johansson, The Hilbert Transform, Master Thesis, Mathematics, Växjö University, 1999.
[26] IEEE Press John Wiley & Sons, 1979.
[27] S. Mitra, *Digital Signal Processing*, 4th ed., McGraw-Hill, 2010.
[28] Xilnix DS240, April 28, 2005, 〈http://www.xilinx.com/ipcenter/catalog/logicore/docs/da_fir.pdf〉.